RSC Advances

PAPER

View Article Online
View Journal | View Issue

Check for updates

Cite this: *RSC Adv.*, 2017, 7, 43812

Time–temperature superposition in the grain and grain boundary response regime of A_2HoRuO_6 (A = Ba, Sr, Ca) double perovskite ceramics: a conductivity spectroscopic analysis

Saswata Halder, *[a] Alo Dutta[b] and T. P. Sinha[a]

Received 27th July 2017
Accepted 4th September 2017

DOI: 10.1039/c7ra08295a

rsc.li/rsc-advances

The pursuit for a universal scaling factor to satisfy the time–temperature superposition principle for grain and grain boundary responses has been explored in the ac conductivity domain for polycrystalline double perovskite oxides A_2HoRuO_6 (AHR; A = Ba, Sr, Ca). The samples show different structural phases, from cubic to monoclinic, with decreasing ionic radii. The degree of distortion in the materials is correlated to the strength of the bonding through the bond valence sum (BVS) formalism. The conductivity spectra for all of the samples obey the power law variation. The contribution of different microstructural domains to the conduction process is established. Thermal variation of the dc resistivity points towards a gradual crossover from nearest neighbour to variable range hopping. The activation energies obtained from the dc conductivity, hopping frequency and relaxation frequency show close correlation between the conduction and relaxation mechanisms. The scaled conductivity curves for AHR display the presence of two different conduction processes with dissimilar activation energies in the grain boundary and the grain response regimes. It is thus concluded that a single scaling parameter is insufficient to satisfy the time temperature superposition principle universally when two different thermally activated regions are present simultaneously in the materials.

1. Introduction

The solid state chemistry of 4d Ru-based materials has always been an intriguing subject to the scientific community since the discovery of spin-glass behavior in Sr_2FeRuO_6.[1–3] Ru-based double perovskite oxides (DPOs) have emerged as a fertile ground for the exploration of novel transport phenomena resulting from a delicate balance between localised and delocalised electron behaviour driven by spin–orbit coupling (SOC), coulombic interactions (U) and crystal field interactions.[4–15] In the case of DPO with Ru at the B-site, an increase in orbital overlap with the decrease in unit cell volume has been shown to increase the Ru-d electron delocalisation.[16] The sensitivity of the narrow itinerant 4d band of Ru is dependent on the degree of hybridization between the Ru-t_{2g} and the O-2p orbitals along with the distortions present in the octahedral environment of Ru. Since the B-site of a DPO provides a dominant influence in determining the transport properties of the material, Ru at the octahedral B-site plays a major role in determining the electrical and magnetic properties of the host material. This research article focusses on the octahedral distortion induced electrical response of a specific DPO series A_2HoRuO_6 (AHR; A = Ba, Sr, Ca) in the radio frequency regime.

The crystal and magnetic properties of AHR have been studied in details by many research groups. The crystal structure and magnetic properties of Ba_2HoRuO_6 (BHR) was studied by Hinatsu *et al.*[17] The crystal structure was reported to be cubic *Fm*3*m*. The magnetic susceptibility and specific heat measurements showed the presence of two anomalies at 22 K and 50 K due to the magnetic ordering of Ho^{3+} ions and Ru^{5+} ions respectively. The crystal structure and magnetic properties of Sr_2HoRuO_6 (SHR) was explored by Doi *et al.*[18] SHR was shown to crystallize in a monoclinic space group $P2_1/n$, with an antiferromagnetic transition at 36 K and a high Weiss constant. Neutron diffraction measurements suggested that both BHR and SHR have long range antiferromagnetic ordering with a type I arrangement of both the Ho^{3+} and Ru^{5+} ions. The crystal structure of Ca_2HoRuO_6 (CHR) was reported by Battle *et al.*[19] to have a partial distribution of both Ca^{2+} and Ho^{3+} ions at both the A and B sites respectively. In the case of CHR, Ru^{5+} ions adopted a type I antiferromagnetic ordering at 4.2 K but no evidence of long range magnetic ordering among the Ho^{3+} ions was observed.

Although reports about the magnetic properties of AHR exist in literature, the knowledge about the ac electrical properties

---

[a] *Department of Physics, Bose Institute, 93/1, Acharya Prafulla Chandra Road, Kolkata 700009, India. E-mail: saswata.h88@gmail.com*

[b] *Department of Condensed Matter Physics and Material Sciences, S. N. Bose National Centre for Basic Sciences, Block-JD, Sector-III, Salt Lake, Kolkata 700098, India*

and dynamics of charge carriers in the radio frequency region remain a scarcity in literature. An understanding of the charge carrier dynamics is imperative in order to tailor the electrical properties of materials. The charge carrier dynamics can be extracted with the help of either the conductivity spectra[20] or the modulus spectra.[21] The conductivity spectra follow a power law behaviour[22,23] consisting of a frequency independent (dc) region and a frequency dependent dispersive component. The cross-over frequency which is also known as the hopping frequency provides the transition from the dc to the ac region. The hopping frequency can be related to the dc conductivity through the Nernst–Einstein relation (eqn (1)) and can be used to estimate the thermal variation of charge carrier concentration

$$\sigma_{\mathrm{dc}} = en_{\mathrm{c}}\mu = \frac{n_{\mathrm{c}}e^2\gamma\lambda^2}{kT}\omega_{\mathrm{H}} \tag{1}$$

where n_c is the concentration of the mobile charges, μ is their mobility, e is the electronic charge, γ is a geometrical factor related to hopping and λ is the hopping distance. The scaling behaviour of the conductivity spectra of glasses and amorphous materials have been studied previously.[24,25] But very few studies exist that explores the dynamics of charge carriers in polycrystalline materials. Saha *et al.* found the validity of time–temperature superposition (TTSP) for polycrystalline $BaFe_{0.5}Nb_{0.5}O_3$ at low temperatures through the scaling of the ac conductivity spectra.[26] TTSP is satisfied by the scaling behaviour of the ac conductivity spectra when the conductivity isotherm collapses into a single master curve with respect to the specified scaling parameters[27] showing the temperature independence of the conduction mechanism. The temperature dependence is incorporated in the increase of the charge carrier density without having any direct effect on the conduction mechanism. However, the validation of TTSP at the different microstructural domains for polycrystalline samples has been rarely studied. The TTSP can be mathematically expressed as,[28,29]

$$\frac{\sigma'(\omega)}{\sigma_{\mathrm{dc}}} = F\left(\frac{\omega}{\omega_{\mathrm{s}}}\right) \tag{2}$$

where the scaling factor F is independent of temperature and ω_s is the scaling parameter.[30–32] In this article, the charge carrier dynamics of AHR is comprehensively discussed in the measured temperature range in the realms of ac conductivity and electric modulus formalisms. The validity of the TTSP is investigated in the various microstructural response regimes through the scaling of the ac conductivity spectra.

2. Experimental details: material synthesis and characterization

AHR was synthesized using the standard solid state reaction method. Powders of $BaCO_3$ (Loba Chemie, 99% pure), $SrCO_3$ (Loba Chemie, 99% pure), $CaCO_3$ (Loba Chemie, 99% pure), Ho_2O_3 (Sigma-Aldrich, 99% pure) and RuO_2 (Alfa-Aesar, 99% pure) were taken in appropriate proportions in accordance with stoichiometric analysis. The ingredients were mixed homogeneously in an agate mortar by hand grinding in dry form and then in acetone medium at periodic intervals for 10 h. The mixture was initially raised to 1300 °C in an alumina crucible at a heating rate of 260 °C h^{-1}, then calcined at 1300 °C for 10 h and brought to room temperature at the cooling rate of 90 °C h^{-1}. In the next step, the calcined powder was pelletized into discs of 8 mm diameter and 1.7 mm thickness using polyvinyl alcohol as binder. Finally, the discs were raised to 1350 °C at a heating rate of 270 °C h^{-1}, sintered at 1350 °C for 10 h followed by cooling down to room temperature at the rate of 1.6 °C min^{-1}.

The X-ray diffraction (XRD) patterns of the samples were collected using X-ray powder diffractometer (Rigaku Miniflex II diffractometer, Tokyo, Japan) using CuK_α radiation in the 2θ range of 10–80° at a scanning rate of 0.02° per step. Rietveld refinement of the XRD data is performed by the Fullprof code.[33] For dielectric measurements, the sintered pellets were polished on both the sides and kept between two thin gold electrodes. The scanning electron micrographs (SEM) of BHR, SHR and CHR were obtained at magnifications of 24 000, 14 000 and 10 000 respectively by the FEI Quanta 200 scanning electron microscope. The complex impedance (Z^*), phase angle (ϕ) and conductance (G) were measured using a computer controlled LCR meter (HIOKI-3552, Nagano, Japan) in the frequency range from 42 Hz to 5 MHz and temperature range 303 K to 613 K at an oscillation voltage of 1.0 V. The temperature was controlled by a Eurotherm 2216e programmable temperature controller connected with the oven and each measured temperature was kept constant with an accuracy of ±1 K. The error in the experimental data was found to be less than the symbol size used in plotting the experimental data.

3. Results and discussions

3.1. Structural characterization

The room temperature XRD patterns of BHR, SHR and CHR are shown in Fig. 1(a)–(c) respectively. The structural and fitted parameters for BHR, SHR and CHR are given in Table 1. The Rietveld refinement of the XRD pattern of BHR shows a cubic phase with space group *Fm*3*m*. The space group allows a 1 : 1 ordered arrangement between Ho^{3+} and Ru^{5+} ions. Superlattice lines such as [111] and [311] which arise from the alternate ordering of Ho and Ru sites in BHR are observed in the XRD pattern (Fig. 1(a)). The superlattice reflection [111] and its adjacent fundamental reflection [220] are selected for comparison in order to study the ordering of the B-site in the cubic DPO lattice. The development of ordered geometry at the B-site is given by the ratio of the intensity of the [111] reflection and the [220] fundamental reflection. The occurrence of superlattice reflections ensures a non-zero value of the intensity ratio thereby showing the presence of an ordered B-site. The intensity ratio $I[111]/I[220]$ is found to be 0.04, indicating the ordering in the Ho and Ru site in BHR.[34,35] The degree of ordering within a given compound was determined by the Long Range Order (LRO) parameter: $\mathrm{LRO} = [2x_{\mathrm{B}} - 1]$, where x_B is the fractional occupancy of the B site cation on the predominantly occupied octahedral site. The refinement is done varying the occupancy parameter x_B and the best result is obtained with $x_B = 1$ which implies complete ordering of the B site cations[36] as shown in Fig. 2(a)–(c).

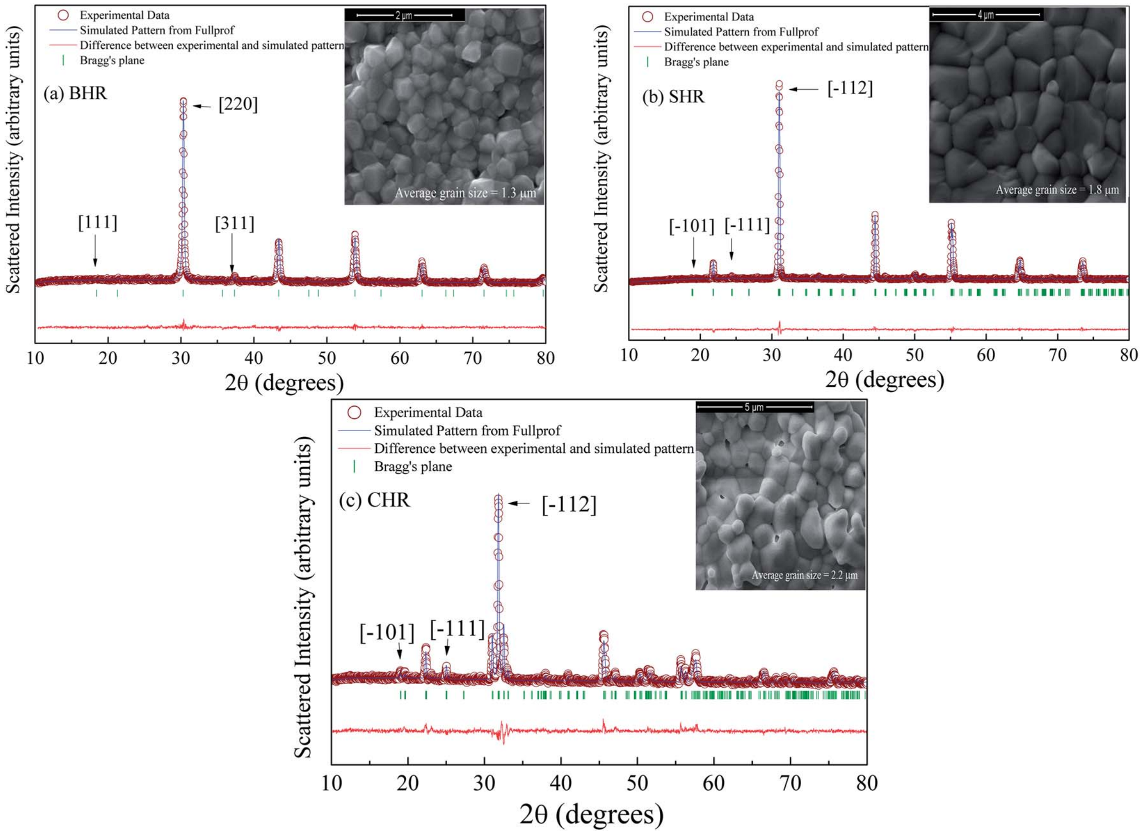

Fig. 1 Room temperature XRD profile of (a) Ba_2HoRuO_6 (BHR), (b) Sr_2HoRuO_6 (SHR) and (c) Ca_2HoRuO_6 (CHR). The SEM images for BHR, SHR and CHR are shown in the inset of the figures.

The XRD profiles of SHR and CHR with monoclinic space group $P2_1/n$ present contrasting features. The XRD pattern of SHR sample in Fig. 1(b) show two superlattice reflection peaks at $2\theta \approx 18^\circ$ $[\bar{1}01]$ and 24° $[\bar{1}11]$ respectively. The degree of site ordering in the monoclinic lattice is given by the intensity ratio $I[\bar{1}01]/I[\bar{1}12]$ of the superlattice reflection peak. This intensity ratio is found to be 0.03, indicating the ordering of Ho and Ru at the B-site in SHR as evident in Fig. 2(d)–(f). The reflection at $2\theta \approx 18^\circ$ $[\bar{1}01]$ is a consequence of the antiphase tilting of the octahedra around the principal 2-fold axis.[37] The other

Table 1 Crystal structure parameters for AHR as obtained from Rietveld refinement of XRD data

	Atoms	Wyckoff	x	y	z	Lattice parameters	Bond length (Å)	Bond angle	χ^2
BHR	Ba	8c	0.25	0.25	0.25	$a = 8.3337$ Å	<Ho–O> = 2.20	<Ho–O–Ru> = 180°	1.22
	Ho	4a	0.00	0.00	0.00		<Ru–O> = 1.95		
	Ru	4b	0.50	0.50	0.50				
	O	24e	0.266(2)	0.00	0.00				
SHR	Sr	4e	0.5017(0)	0.5284(0)	0.2414(0)	$a = 5.7529$ Å	<Ho–O> = 2.21	<Ho–O_1–Ru> = 164°	1.38
	Ho	2c	0.00	0.50	0.00	$b = 5.7739$ Å	<Ru–O> = 1.94	<Ho–O_2–Ru> = 154°	
	Ru	2d	0.50	0.00	0.00	$c = 8.1464$ Å		<Ho–O_3–Ru> = 152°	
	O_1	4e	0.2199(0)	0.2118(0)	−0.0043(0)				
	O_2	4e	0.3051(0)	0.7254(0)	−0.0385(0)	$\beta = 89.87^\circ$			
	O_3	4e	0.4142(5)	−0.0117(5)	0.2329(5)				
CHR	Ca_1	4e	0.5245(2)	0.5682(8)	0.2631(1)	$a = 5.5013$ Å	<Ho_1–O> = 2.44	<Ho_2–O_1–Ru> = 149°	1.82
	Ho_1	4e	0.5245(2)	0.5682(8)	0.2631(1)	$b = 5.7594$ Å	<Ho_2–O> = 2.33	<Ho_2–O_2–Ru> = 151°	
	Ca_2	2c	0.00	0.50	0.00	$c = 7.9333$ Å	<Ru–O> = 1.88	<Ho_2–O_3–Ru> = 152°	
	Ho_2	2c	0.00	0.50	0.00				
	Ru	2d	0.50	0.00	0.00				
	O_1	4e	0.3301(2)	0.2238(2)	−0.063(2)				
	O_2	4e	0.3260(1)	0.7299(1)	−0.043(9)	$\beta = 90.17^\circ$			
	O_3	4e	0.4093(1)	−0.0054(8)	0.2356(8)				

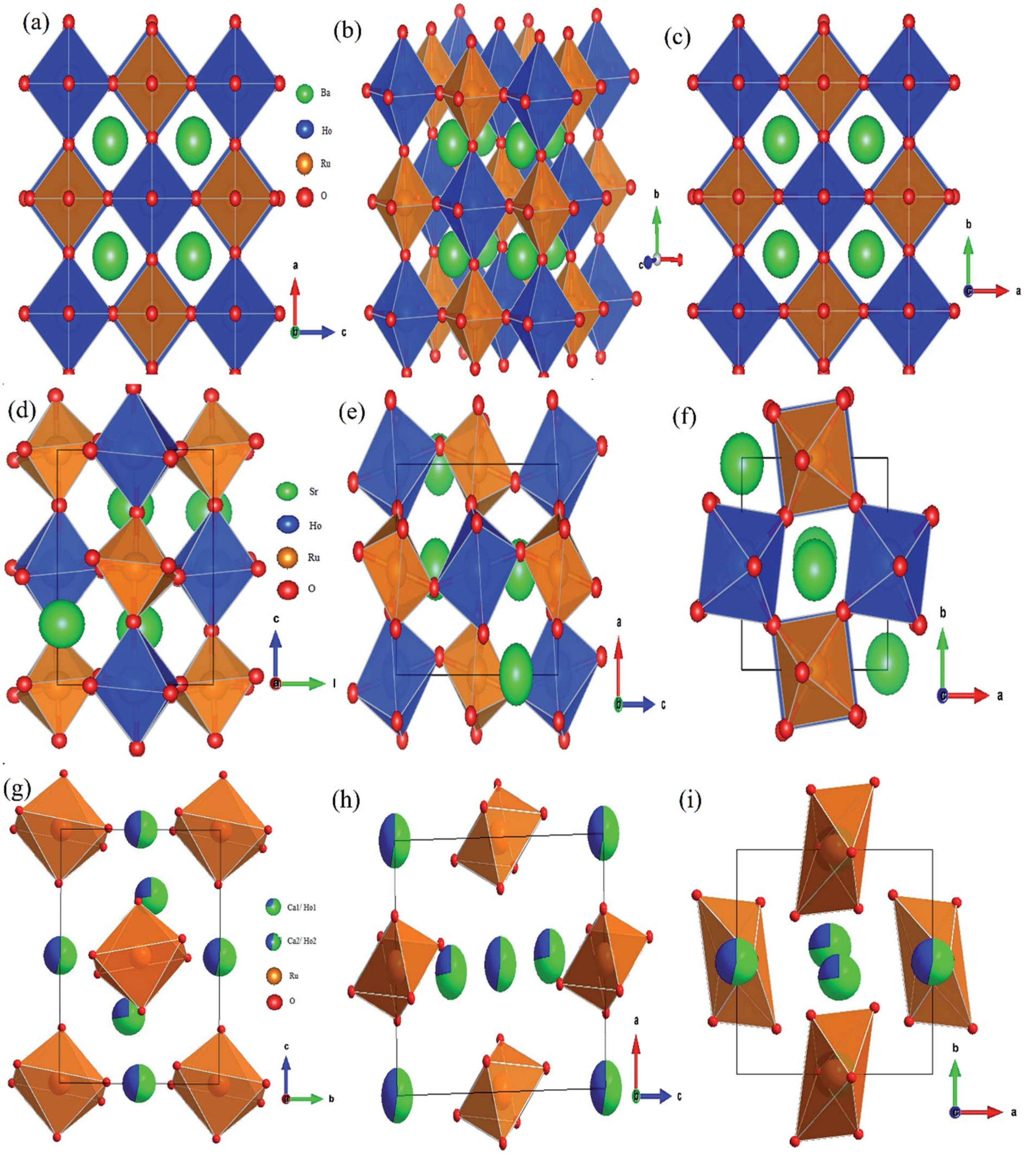

Fig. 2 Crystal structures at different orientations for (a)–(c) Ba_2HoRuO_6 (BHR), (d)–(f) Sr_2HoRuO_6 (SHR) and (g)–(i) Ca_2HoRuO_6 (CHR).

reflection located at $2\theta \approx 24°$ $[\bar{1}11]$, arises from the in-phase tilt of the octahedra around the primitive axis.[38] The total intensity of the [002] and [110] reflections are significantly decreased when Ca replaces Sr at the A-site as evident from the comparative study of the XRD profiles of SHR and CHR thus showing the A-site is partially occupied by the Ca^{2+} ions giving rise to a different cationic distribution in CHR as compared to SHR. The cationic distributions that best fits the intensity profile of CHR is Ca^{2+}/Ho^{3+} (4e), Ca^{2+}/Ho^{3+} (2d), Ru^{5+} (2c) corresponding to the formula $(Ca_{1.46}Ho_{0.54})(Ca_{0.54}Ho_{0.46})RuO_6$ showing the partial occupation of the Ca and Ho ions at both the A-site and the B-site of the double perovskite in agreement to the suggestion by Battle *et al.*[19] There exists no cationic ordering between the Ca^{2+} and Ho^{3+} ions at either of the A or B-sites although the Ca^{2+}/Ho^{3+} ions form a 1 : 1 ordered arrangement with the Ru^{5+} ions at the B-site as seen in Fig. 2(g)–(i). The intensity ratio of the superlattice reflection in CHR ($I[011]/I[\bar{1}12]$) is found to be 0.12 which also signifies the B-site ordering in the sample.

Bond valence sum (BVS) for AHR are given in Table 2. The BVS of the A^{2+} cations are significantly less than 2.0 which

Table 2 Bond valence sum (BVS) and activation energies of grain and grain boundary from Arrhenius fit of thermal variation of dc conductivity, hopping frequency and relaxation frequency

	Atoms	Charge	BVS	$E_a^{\sigma_{dc}}$ (eV)	$E_a^{\omega_H}$ (eV)	$E_a^{\omega_m}$ (eV)
BHR	Ba	+2	1.992	$E_a^t = 0.27$ eV	$E_a^t = 0.26$ eV	$E_a^{gb} = 0.25$ eV
	Ho	+3	3.573			
	Ru	+5	5.240			
SHR	Sr	+2	1.783	$E_a^t = 0.31$ eV	$E_a^t = 0.29$ eV	$E_a^{gb} = 0.29$ eV
	Ho	+3	3.423			
	Ru	+5	5.379	$E_a^g = 0.22$ eV		
CHR	Ca_1	+2	1.382	$E_a^t = 0.37$ eV	$E_a^t = 0.35$ eV	$E_a^{gb} = 0.31$ eV
	Ho_1	+3	2.106			
	Ca_2	+2	1.801	$E_a^g = 0.26$ eV		
	Ho_2	+3	2.662			
	Ru	+5	5.392			

demonstrates that the average A–O distances are longer than optimal.[39] The BVS for Ba^{2+} and Sr^{2+} in BHR and SHR is 1.992 and 1.783 respectively. The Ca^{2+} (BVS = 1.382) at the A-site is comparatively more under-bonded than the Ca^{2+} (BVS = 1.801) at the B-site showing that the bonding strength in CaO_6 octahedra is more than in the CaO_{12} octahedra. The increased bond valency reflects that the A-site is becoming more convenient for the A^{2+} cation thereby reducing the requirement for octahedral tilting resulting in a more symmetrical crystal structure. The bond lengths and BVS provide further insight into the bonding requirement of the two B-site cations of significant size difference which are distributed in an ordered perovskite structure. In case of BHR and SHR, the Ho^{3+} are over-bonded with the Ho–O bond lengths being shorter than the expected value. In the case of CHR, both Ho atoms are considerably under-bonded which is reflected in the respective bond lengths which are greater than the calculated values. This can be attributed to the increase in the distortion resulting in the lengthening and

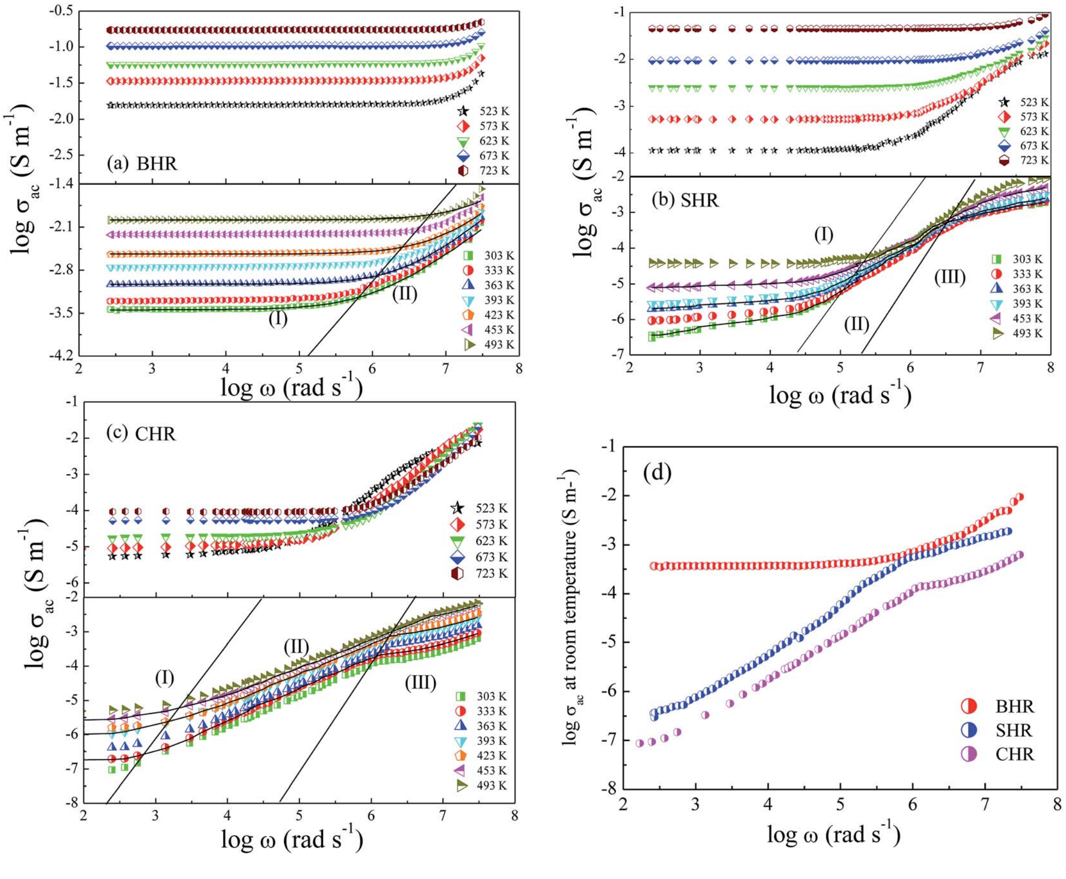

Fig. 3 AC conductivity spectroscopic plot at selected temperatures for (a) Ba_2HoRuO_6 (BHR), (b) Sr_2HoRuO_6 (SHR), (c) Ca_2HoRuO_6 (CHR) and (d) ac conductivity plots for BHR, SHR and CHR at room temperature.

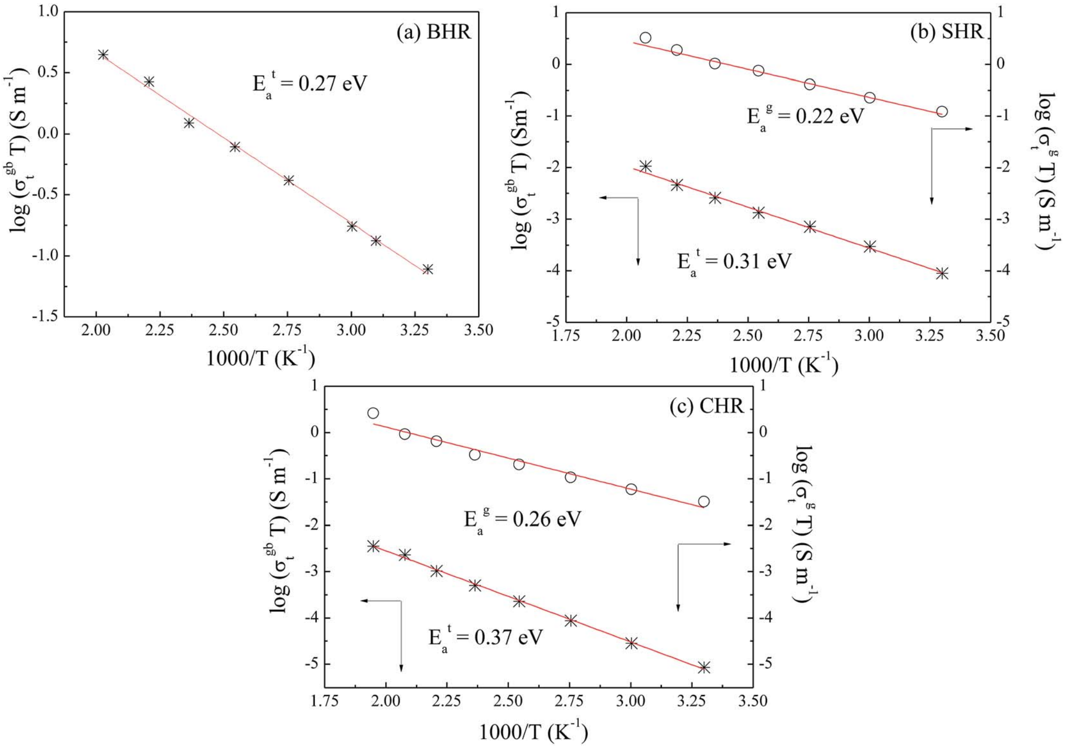

Fig. 4 Thermal variation of dc conductivity (σ_{dc}) for (a) Ba_2HoRuO_6 (BHR), (b) Sr_2HoRuO_6 (SHR) and (c) Ca_2HoRuO_6 (CHR).

shortening of different axes to attain the lowest energy stable crystal structure. The Ru-atom in all three materials are over-bonded as observed from Ru–O bond length which is shorter than the expected value. The Ho–O bond lengths systematically increase whereas the Ru–O bond length decreases as Ca replaces Ba/Sr at the A-site. This shows that with distortion the

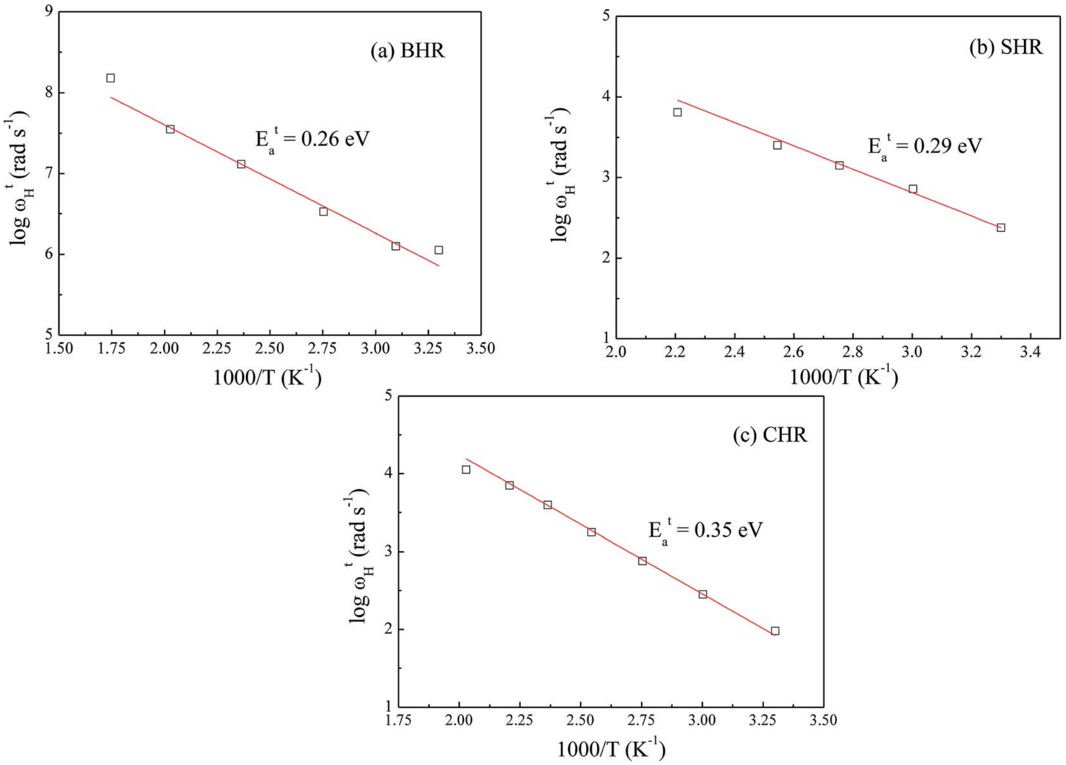

Fig. 5 Thermal variation of hopping frequency (ω_H) at grain boundaries for (a) Ba_2HoRuO_6 (BHR), (b) Sr_2HoRuO_6 (SHR) and (c) Ca_2HoRuO_6 (CHR).

Ho–O axis elongates and Ru–O axis shortens. Although minor variations in determining the BVS values may arise due to the low scattering coefficient of oxygen ions, the BVS formalism still provides a very qualitative analysis of the bonding environment inside AHR. The ease with which any cation pair can form a perovskite structure is expressed in terms of a geometrical quantity known as the tolerance factor (t) given by.[40,41]

$$t = \frac{R_{\mathrm{A}} + R_{\mathrm{o}}}{\sqrt{2}\left[\frac{(R_{\mathrm{Ho}} + R_{\mathrm{Ru}})}{2} + R_{\mathrm{o}}\right]} \tag{3}$$

It predicts that for a given pair of B-site cations (Ho and Ru in the present case) an increase in the size of the A-site cation increases the tolerance factor of the perovskite system. A cubic perovskite structure is obtained for t close to unity, whereas the structure progressively undergoes distortion for lower values of t due to the mismatch of the A-site and B-site ionic radii. The values of the geometric tolerance factor t for BHR, SHR and CHR are calculated to be 1.004, 0.95 and 0.91 respectively, which is in agreement with the cubic structure of BHR and the monoclinic structures for SHR and CHR respectively as shown in Fig. 2(a)–(i). The increased bond valency reflects that the size of the A-site is becoming more suitable for the A^{2+} cation reducing the requirement for octahedral tilting in the perovskite structure resulting in an increase in the symmetry of the materials due to the volumetric resemblance of the BO_6 and AO_{12} octahedra. The crystal structure approaches the higher symmetry configuration as one moves from CHR to BHR reducing the octahedral distortion in the system as is reflected in the <B′–O–B″> bond angles which approach 180°.

The SEM images of the samples are shown in the inset of Fig. 1(a)–(c) for BHR, SHR and CHR respectively. The SEM images indicate high density of the materials as well as uniform distribution of grains of different sizes and shapes in the samples. The average grain size for BHR, SHR and CHR is found to be 1.3 μm, 1.8 μm and 2.2 μm respectively. The density of BHR, SHR and CHR is 7.307 g cc^{-1}, 6.594 g cc^{-1} and 5.897 g cc^{-1} respectively which is 97%, 95% and 94% of the theoretical density.

3.2. Electrical characterization

Dynamical processes in materials are studied by a variety of spectroscopic techniques. Electrical relaxation measurements are commonly used, mostly as a function of frequency, to study the charge dynamics in materials.[42] With the advancement of ac conductivity measurement techniques, impedance analysis has become a widely accepted tool for the characterization of the experimental data. Fig. 3(a)–(c) present the spectroscopic plots of the real part of ac conductivity for BHR, SHR and CHR respectively at selected temperatures. The symbols represent the experimental data and the solid lines represent the fit of the experimental conductivity spectra in accordance to the power law (eqn (4)) suggested by Almond and West:[43,44]

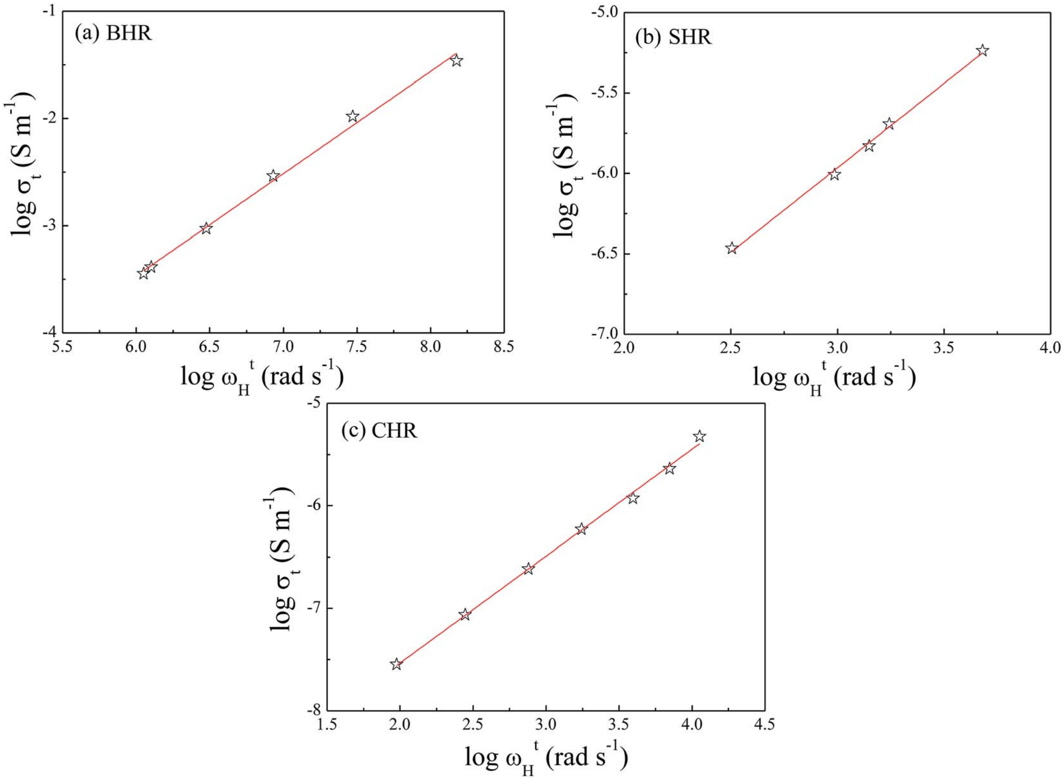

Fig. 6 Correlation between dc conductivity (σ_{dc}) and hopping frequency (ω_H) at grain boundaries for (a) Ba_2HoRuO_6 (BHR), (b) Sr_2HoRuO_6 (SHR) and (c) Ca_2HoRuO_6 (CHR).

$$\sigma'(\omega) = \sigma_{\mathrm{dc}}\left[1 + \left(\frac{\omega}{\omega_{\mathrm{H}}}\right)^{n}\right] \tag{4}$$

In eqn (4), σ_{dc} represents the dc conductivity, ω is the angular frequency, n is the power law exponent describing the electrical relaxation behaviour of the material and ω_{H} represents the hopping frequency of the charge carriers which marks the crossover from long range translational to the dispersive conduction region at $\omega > \omega_{\mathrm{H}}$. In a polycrystalline ceramic system, conductivity relaxation occurs due to grain, grain-boundary and electrode-specimen interface contributions. In absence of electrode polarization, electro-ceramics show the presence of plateaus and dispersion regions in their conductivity spectra due to the contribution from different microstructural regions.[45–47] The spectroscopic plots for BHR, SHR and CHR have been divided into different regimes revealing different microstructural contribution to the conductivity of the materials. In the case of BHR (Fig. 3(a)), a single plateau in the low frequency region (region I) followed by a dispersion region (region II) is observed. The single plateau can be assigned to the total conductivity of the sample measuring the overall dc conductivity of the sample in the limit $\omega \rightarrow 0$ *i.e.* ($\sigma_{\mathrm{dc}} = \sigma_{\mathrm{t}}(\omega \rightarrow 0)$). The dispersion region can be attributed to the grain boundary relaxation of the sample. In the case of SHR and CHR (Fig. 3(b) and (c)), the presence of another plateau is observed along with regions I and II. This plateau denoted by region III can be assigned to the contribution of the grains to the total conductivity.

The frequency dependent conductivity can be interpreted in terms of the grain boundary conductivity and jump relaxation model.[48,49] In this model, the total conductivity, which is a measure of the dc conductivity at $\omega \rightarrow 0$, is caused by the long range translational motion of charge carriers between localised sites. The ac conductivity in the dispersion regime is caused by the correlated backward and forward hopping motion of the charge carriers which can be visualised as a competition between two relaxation processes; successful and unsuccessful hopping of charge carriers. The conductivity of BHR is found to be greater than SHR and CHR for a particular temperature. The conductivity of the materials are enhanced with increase in temperature due to the thermal activation of charge carriers across the energy gap. As previously mentioned the conduction in AHR is dependent on the degree of hybridization between the Ru t_{2g} and O-2p orbitals along with the distortions present in the Ru octahedral surroundings. As Ca replaces Ba and Sr at the A-site of the perovskite lattice, the degree of distortion increase which lowers the hybridization between the Ru t_{2g} and O-2p orbitals. The decrease in electron delocalisation around the Ru-atom inhibits the facilitative transfer of electrons from the valence band to the conduction band. Thus the conductivity decreases as the distortions in the octahedra increase from BHR ($t = 1.004$) to CHR ($t = 0.91$). It seems plausible that due to the

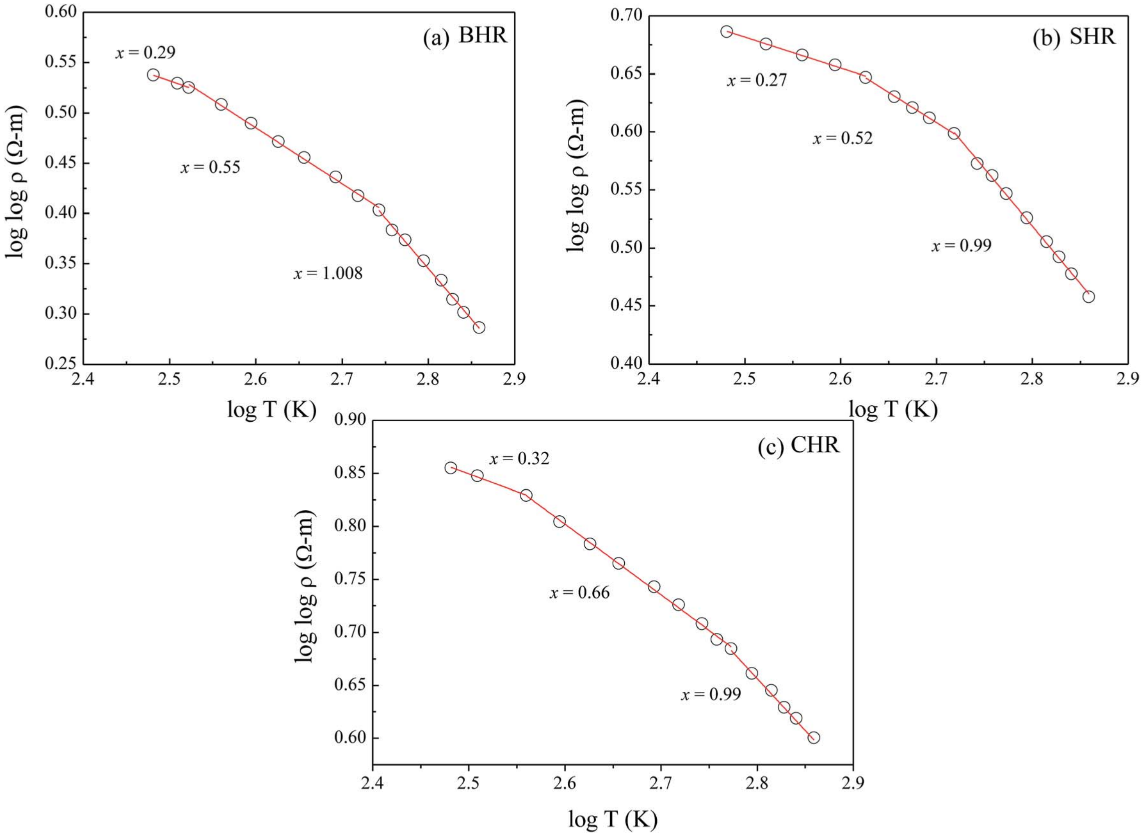

Fig. 7 Temperature dependence of electrical resistivity (a) Ba_2HoRuO_6 (BHR), (b) Sr_2HoRuO_6 (SHR), and (c) Ca_2HoRuO_6 (CHR).

ordered arrangement of the octahedra, the complete electron delocalization of Ru cation could be inhibited by the HoO_6 octahedra by the physical separation of the two successive RuO_6 octahedra. In AHR, every second Ru is substituted by Ho forming a rock-salt arrangement and disrupting the Ru–O perovskite motif of intersecting 1D chains. As a result the AHR shows more localised electrical behaviour than most of the parent perovskite derived ruthenates.[50–54]

If the dc conductivity is Arrhenius activated, then $\sigma_t \propto \frac{E_a{}^\sigma}{kT}$, where $E_a{}^\sigma$ is the activation energy for dc conductivity, k represents the Boltzmann constant and T is the absolute temperature. For a fixed number of sites N and fixed hopping length R, it can be shown that the hopping frequency also varies as $\omega_H \propto \frac{E_a{}^\omega}{kT}$.[27] If the power law exponent 'n' is independent or a weakly varying function of temperature then ω_H activates with the same energy as σ_t. In the present study, 'n' is found to be weakly temperature dependent. Arrhenius representation of dc conductivity (σ_t) and hopping frequency (ω_H) for BHR, SHR and CHR are shown in Fig. 4 and 5 respectively. The activation energy for grain boundary is found to be higher than the activation energy for grains. Both dc conductivity (σ_t) and hopping frequency (ω_H) show identical profiles with a linear behaviour in the investigated temperature range. The activation energies for σ_t and ω_H, determined from the slope of the linear fit to the experimental data, are given in Table 2. It is observed that the activation energies of dc conductivity are close to the activation energies of hopping frequency for all the three samples showing that σ_t is proportional to ω_H. The value of the activation energy for bulk conductivity suggests that the conduction mechanism occurs due to the hopping of small polarons. In general, an activation energy of more than 0.2 eV is reminiscent of polaronic conduction of holes. On this basis it can be inferred that p-type carriers are responsible for the charge conduction in AHR.[55,56]

To examine the correlation between dc conductivity (σ_t) and hopping frequency (ω_H), the logarithmic plot are drawn between these two parameters as shown in Fig. 6(a)–(c). The figures show a near linear nature with a slope of almost unity indicating a power law dependency of the form $\sigma_t \propto \omega_H{}^n$ where 'n' is the slope of the graph. This implies that the dc and ac conductivity are correlated in AHR.[57]

The electrical resistivity ρ can be deduced from the dc conductivity σ_t using the relation $\rho = 1/\sigma_t$. To understand the possible conduction mechanism, it is customary to investigate the variation of electrical resistivity with temperature. The results are analysed in terms of the hopping models namely, (i) nearest neighbour hopping or small polaron hopping (SPH) and

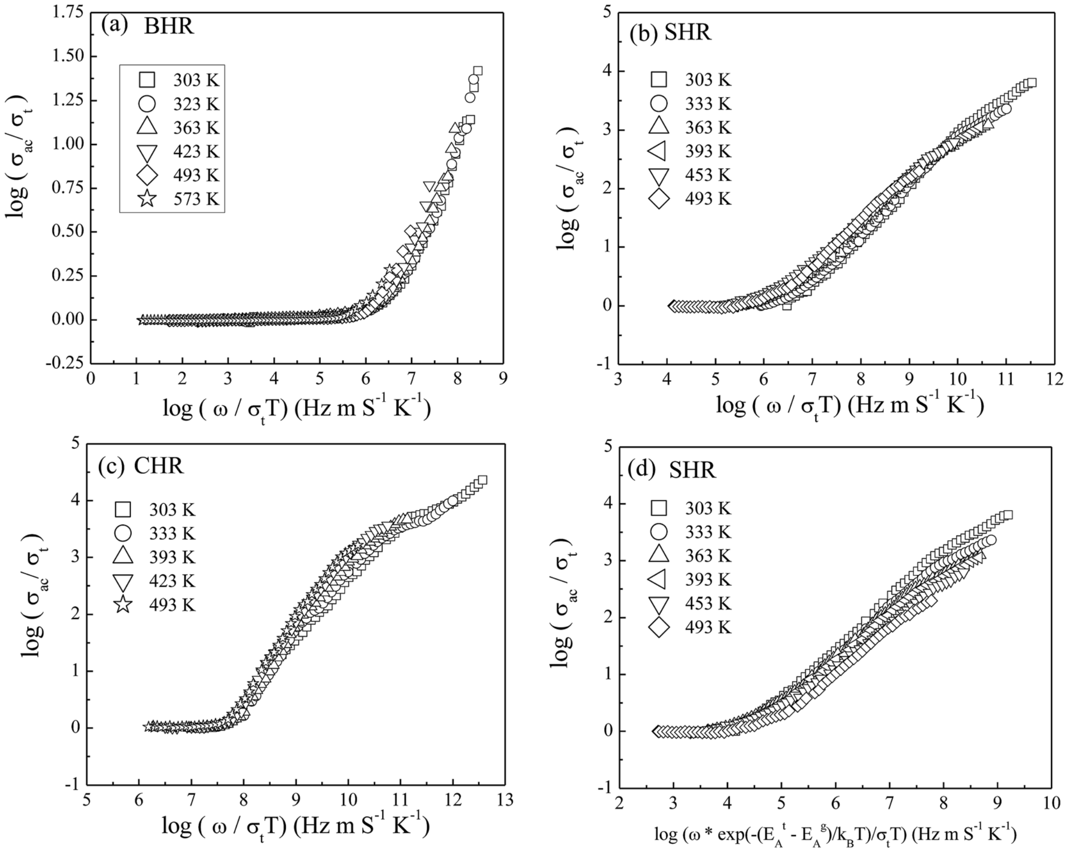

Fig. 8 Summerfield scaling of ac conductivity for (a) Ba_2HoRuO_6 (BHR), (b) Sr_2HoRuO_6 (SHR), (c) Ca_2HoRuO_6 (CHR) and (d) scaling of ac conductivity for SHR with frequency axis scaled by $\frac{\sigma_t T}{e^{\frac{-(E_a^t - E_a^g)}{kT}}}$.

(ii) variable range hopping (VRH).[58,59] The general form of the hopping equation can be written as $\rho \propto e^{\left(\frac{A}{T}\right)^x}$ where $A = T_o$ and $x = 0.25$ represents VRH whereas $A = E_a/k_B$ and $x = 1$ describes the nearest neighbour hopping limit. In order to obtain the exponent 'x' which determines the nature of the hopping process, a plot of log(log ρ) *vs.* log T is shown in Fig. 7(a)–(c) for BHR, SHR and CHR respectively. The slope of the graph determines the value of the exponent 'x'.[60] In all the three materials, the high temperature domain is dominated by the nearest neighbour hopping process ($x \sim 1$) with a gradual cross-over towards variable range hopping limit near room temperature ($x \sim 0.30$). With further decrease in temperature, the VRH limit of $x \sim 0.25$ should be achieved.

To gain valuable insight into the temperature dependence of the conduction mechanism and the response of grains and grain boundaries to the conductivity, the scaling behaviour of frequency dependent conductivity has been performed. In the present study, two different scaling formalisms, Summerfield scaling[61] and Ghosh scaling,[62,63] have been applied to perform the scaling of the conductivity spectroscopic plots. The conductivity axis of the ac conductivity spectra for BHR, SHR and CHR is scaled by the dc conductivity (σ_t) whereas the frequency axis is scaled by $\omega_s = \sigma_t T$ and $\omega_s = \omega_H$ as shown in Fig. 8(a)–(c) and 9(a)–(c) respectively. The ac conductivity spectra for BHR, SHR and CHR are superimposed into a single master curve at the grain boundary region although in the grain response region the ac conductivity data do not collapse into a single master curve. It shows that the relaxation processes at the grain boundary region follow the time–temperature superposition principle (TTSP). However, the deviation of the scaled conductivity curves at the grain region implies that the relaxation phenomena in the grains are different from that in the associated grain boundary response regions. The grain boundaries require higher activation energy than the grains as is evident from Table 2. This difference is in agreement with the dissimilar activation energies of the grains and the grain boundaries ($\Delta E = E_a^t - E_a^g = 0.09$ eV for SHR and 0.11 for CHR). The higher activation energy of the grain boundary conductivity can be due to the combination of a number of serial barriers in the interfacial region and therefore the total conductivity is dictated by the grain boundary impedance. The parameters, such as the diffusion coefficient (D), which affect the bulk and grain conductivity can be obtained from the differently activated response regions. In order to consider the activation energy difference between the bulk and grain interiors the frequency axis has been scaled by the parameter $\frac{\sigma_t T}{e^{\frac{-(E_a^t - E_a^g)}{kT}}}$ and

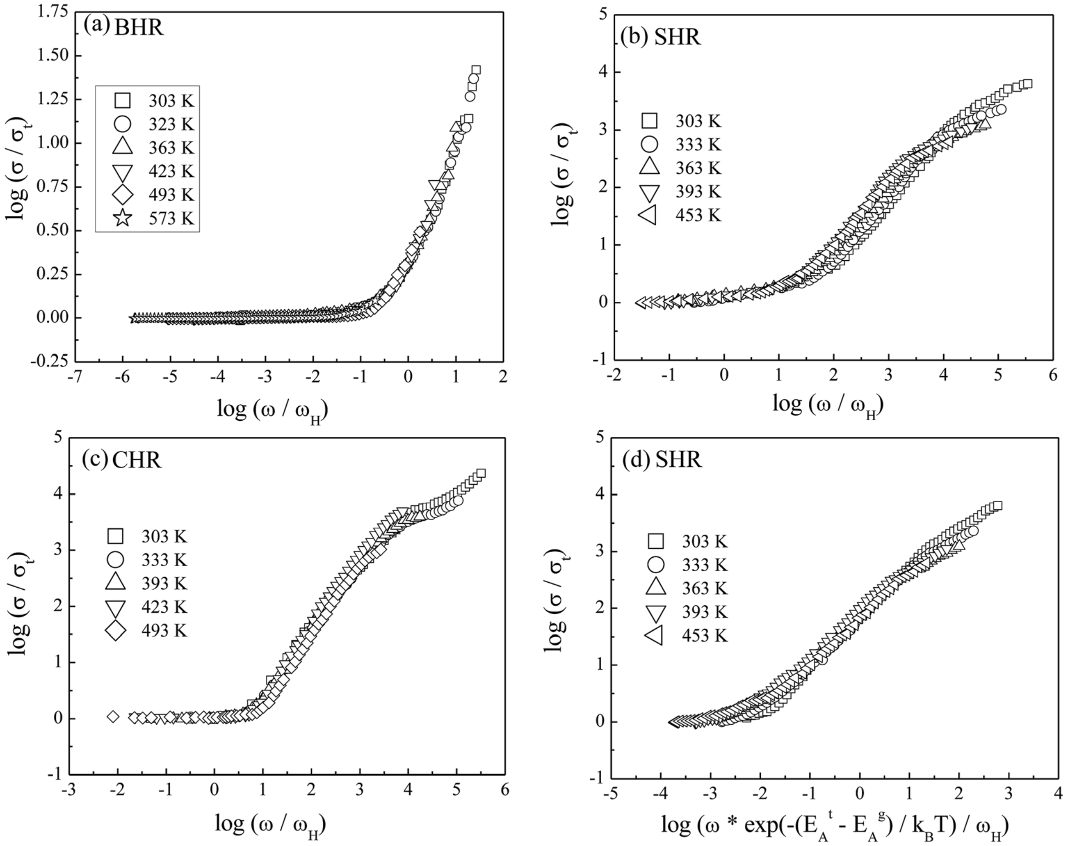

Fig. 9 Scaling of ac conductivity according Ghosh formalism for (a) Ba_2HoRuO_6 (BHR), (b) Sr_2HoRuO_6 (SHR), (c) Ca_2HoRuO_6 (CHR) and (d) scaling of ac conductivity for SHR with frequency axis scaled by $\frac{\omega_H}{e^{\frac{-(E_a^t - E_a^g)}{kT}}}$.

$\frac{\omega_{\mathrm{H}}}{e^{\frac{-(E_{\mathrm{a}}^{\mathrm{t}}-E_{\mathrm{a}}^{\mathrm{g}})}{kT}}}$ (ref. 64) for SHR as shown in Fig. 8(d) and 9(d) respectively. The scaled grain boundary curves are superimposed into a single curve whereas the grain response curve deviate more than previously. The factor $e^{\frac{-(E_{\mathrm{a}}^{\mathrm{t}}-E_{\mathrm{a}}^{\mathrm{g}})}{kT}}$ compensates for the different energy barriers that the mobile ion encounters between the grain boundaries and the grain regions during its percolation. The conductivity scaled isotherms for BHR, SHR and CHR show that the scaling formalism with $\omega_{\mathrm{s}} = \omega_{\mathrm{H}}$ provides a better superposition than the scaling formalism with $\omega_{\mathrm{s}} = \sigma_{\mathrm{t}}T$ due to the fact that σ_{t} has a power law dependence on ω_{H}.

Previous studies have revealed that some school of thought prefer the use of electric modulus formalism in the interpretation of the conduction dynamics by eliminating the electrode polarization effect. The electric modulus formalism was first introduced by Macedo *et al.*[65] in exploring the space-charge relaxation phenomena and is used in conjunction with the impedance and permittivity formalisms to differentiate between the grain and grain boundary regions and to recognize the microscopic processes responsible for localized dielectric relaxations and long-range conductions.[66,67] Fig. 10(a)–(c) display the spectroscopic plots for the imaginary component of electric modulus, M'', at selected temperatures for BHR, SHR and CHR respectively. BHR displays a single relaxation peak in the entire frequency domain whereas both SHR and CHR have two relaxation peaks, one at low frequency due to grain boundary response and the other at high frequency due to the grain response.[68] The M'' peaks are much broader than an ideal Debye peak showing that the relaxation behaviour is non-ideal and the relaxation times are distributed. The increase in frequency as one approaches the peak from the left facilitates the mobility of the charge carriers and represents a region of long range conduction. To the right of the peak, localized forward backward hopping motion occurs as the charge carriers are confined to trapped centres due to their decreased mobility.[69,70] With increase in temperature charge carrier dynamics is boosted with a decrease in relaxation time which manifests itself as a shift in the relaxation frequency (ω_{m}) towards the higher frequency side. A natural conclusion thus follows that the relaxation process is thermally activated with charge carrier hopping determining the conduction dynamics in AHR.

The scaling behaviour of M'' has been performed to obtain an insight into the thermally influenced relaxation dynamics of AHR.[71] The insets of Fig. 10(a)–(c) provide the scaled spectra in which each axis has been scaled by its corresponding peak value obtained from the relaxation maxima at individual temperatures. The figures show that the modulus spectra at different temperatures nearly collapse into a single master curve at the grain boundary response regime, whereas the grain response domain shows a deviation from the scaling behaviour. Similar nature was also obtained from the conductivity scaling behaviour. This indicates that the dynamical process controlling the

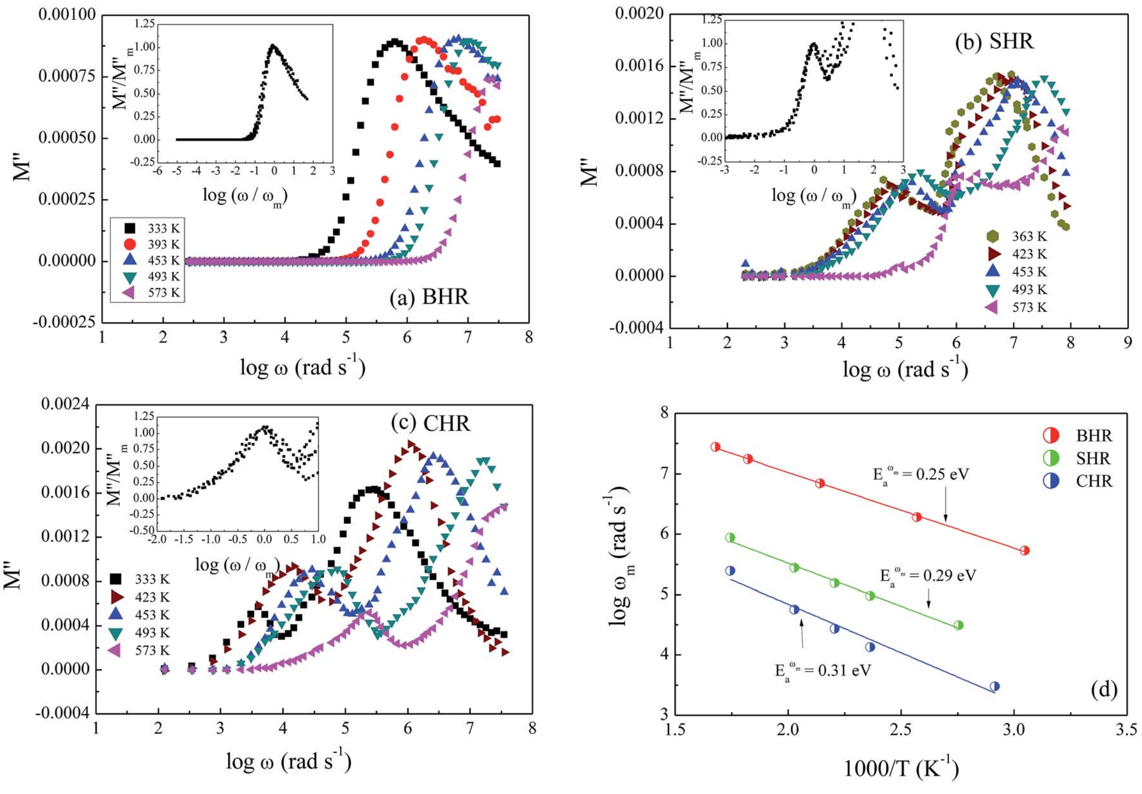

Fig. 10 Frequency dependent electric modulus (M'') for (a) Ba_2HoRuO_6 (BHR), (b) Sr_2HoRuO_6 (SHR) and (c) Ca_2HoRuO_6 (CHR). The insets show the scaling behaviour. (d) Thermal variation of relaxation frequency (ω_{m}) for BHR, SHR and CHR.

conductivity relaxation at the grain boundaries is the same over the entire temperature range although it deviates greatly from the conductivity relaxation dynamics at the grain region. It is therefore concluded that there exists no single scaling parameter that can account for the validation of the time–temperature superposition principle when two dissimilar thermally activated processes are simultaneously present within a material.

Fig. 10(d) represents the thermal variation of relaxation frequency (ω_m) for AHR. The activation energies obtained from the linear fit of the experimental data are 0.25 eV, 0.29 eV and 0.31 eV for BHR, SHR and CHR respectively. A comparison of the activation energies of all the samples for dc conductivity (σ_t), hopping frequency (ω_H) and relaxation frequency (ω_m) show that the values lie close to each other. The close proximity of the values of E_H and $E_{\omega_{max}}$ indicate that the hopping frequency and the relaxation frequency provide the limiting bound to the crossover from short range hopping to long range percolation.

4. Conclusion

A comprehensive quantitative investigation of electrical conduction for polycrystalline double perovskite oxides A_2HoRuO_6 (AHR; A = Ba, Sr, Ca) prepared by solid state technique has been presented over the temperature range of 303–613 K and frequency range 42 Hz to 5 MHz. The room temperature XRD data confirmed the single phase formation of all the materials. The bond valence sum (BVS) formalism correlates the degree of octahedral distortion to the strength of the bonding of the A-site cation. The conductivity spectra for AHR follow a power law variation. The contributions of the different microstructural regimes to the conduction mechanism are observed in the conductivity spectra. The dc conductivity and the hopping frequency are correlated in a power law form. The activation energy of the materials in the grain boundary lies in the range of 0.27–0.37 eV whereas the grain response region have energies of 0.22–0.26 eV. The polaronic conduction mechanism shows a gradual crossover from the nearest neighbour hopping to the variable range hopping mechanism with decrease in temperature. The electric modulus spectra show a thermally activated conduction mechanism. The activation energies obtained from the linear fit of the thermal variation of relaxation frequency (ω_m) are in close proximity to the activation energies obtained from the hopping frequencies (ω_H) showing that both (ω_m) and (ω_H) are correlated. Our investigations show that the time temperature superposition principle using the conductivity scaling formalism is valid only at the specific microstructural response domains and not universally. Hence, we conclude if two electroactive regions have simultaneous dissimilar thermally activated conduction processes in them then there exists no single scaling parameter that can account for the time–temperature superposition principle (TTSP) universally.

Conflicts of interest

There are no conflict of interests to declare.

Acknowledgements

Alo Dutta thanks the Department of Science and Technology of India for providing financial support through DST Fast Track Project under grant no. SR/FTP/PS-175/2013.

References

1 P. D. Battle, T. C. Gibb, C. W. Jones and F. Studer, Spin-Glass Behavior in Sr_2FeRuO_6 and $BaLaNiRuO_6$: A Comparison with Antiferromagnetic $BaLaZnRuO_6$, *J. Solid State Chem.*, 1989, **78**, 281.

2 J. Chang, K. Lee, M. H. Jung, J. H. Kwon, M. Kim and S. K. Kim, Emergence of Room-Temperature Magnetic Ordering in Artificially Fabricated Ordered-Double-Perovskite Sr_2FeRuO_6, *Chem. Mater.*, 2011, **23**, 2693.

3 T. C. Gibb, A study of superexchange interactions in the perovskite Sr_2FeRuO_6 by Monte Carlo analysis, *J. Mater. Chem.*, 2005, **15**, 4015.

4 B. Ranjbar, E. Reynolds, P. Kayser and B. J. Kennedy, Structural and Magnetic Properties of the Iridium Double Perovskites $Ba_{2-x}Sr_xYIrO_6$, *Inorg. Chem.*, 2015, **54**, 10468.

5 P. Kayser, B. J. Kennedy, B. Ranjbar, J. A. Kimpton and M. Avdeev, Spin–Orbit Coupling Controlled Ground State in the Ir(v) Perovskites A_2ScIrO_6 (A = Ba or Sr), *Inorg. Chem.*, 2017, **56**, 2204.

6 L. T. Corredor, G. Aslan-Cansever, M. Sturza, K. Manna, A. Maljuk, S. Gass, T. Dey, A. U. B. Wolter, O. Kataeva, A. Zimmermann, M. Geyer, C. G. F. Blum, S. Wurmehl and B. Buchner, Iridium double perovskite Sr_2YIrO_6: A combined structural and specific heat study, *Phys. Rev. B*, 2017, **95**, 064418.

7 G. J. Nilsen, C. M. Thompson, G. Ehlers, C. A. Marjerrison and J. E. Greedan, Diffuse magnetic neutron scattering in the highly frustrated double perovskite Ba_2YRuO_6, *Phys. Rev. B: Condens. Matter Mater. Phys.*, 2015, **91**, 054415.

8 A. A. Aczel, D. E. Bugaris, L. Li, J.-Q. Yan, C. de la Cruz, H.-C. zur Loye and S. E. Nagler, Frustration by competing interactions in the highly distorted double perovskites La_2NaBO_6 (B = Ru, Os), *Phys. Rev. B: Condens. Matter Mater. Phys.*, 2013, **87**, 014435.

9 C. M. Thompson, C. A. Marjerrison, A. Z. Sharma, C. R. Wiebe, D. D. Maharaj, G. Sala, R. Flacau, A. M. Hallas, Y. Cai, B. D. Gaulin, G. M. Luke and J. E. Greedan, Frustrated magnetism in the double perovskite La_2LiOsO_6: A comparison with La_2LiRuO_6, *Phys. Rev. B*, 2016, **93**, 014431.

10 H.-R. Fuh, Y.-P. Liu, S.-H. Chen and Y.-K. Wang, Electronic structures of compensated magnetism in double perovskites $A_2CrRu(Os)O_6$ (A = Si, Ge, Sn, and Pb) from ab initio calculations, *J. Alloys Compd.*, 2013, **547**, 126.

11 B. Ranjbar, A. Pavan, B. J. Kennedy and Z. Zhang, Structural and magnetic properties of the ruthenium double perovskites $Ba_{2-x}Sr_xYRuO_6$, *Dalton Trans.*, 2015, **44**, 10689.

12 P. D. Battle, J. B. Goodenough and R. Price, The Crystal Structures and Magnetic Properties of Ba_2LaRuO_6 and Ca_2LaRuO_6, *J. Solid State Chem.*, 1983, **46**, 234.

13 P. D. Battle and C. W. Jones, The crystal and magnetic structures of Sr_2LuRuO_6, Ba_2YRuO_6, and Ba_2LuRuO_6, *J. Solid State Chem.*, 1989, **78**, 108.

14 P. D. Battle and W. J. Macklin, The crystal and magnetic structures of Ca_2YRuO_6 and the electronic properties of the series $M_2{}^{2+}X^{3+}Ru^{5+}O_6$ (M = Ca, Sr, Ba; X= La, Y), *J. Solid State Chem.*, 1984, **54**, 245.

15 A. V. Powell, J. G. Gore and P. D. Battle, The magnetic properties of iridium in mixed-metal oxides, *J. Alloys Compd.*, 1993, **201**, 73.

16 A. Maignan, C. Martin, M. Hervieu and B. Raveau, Ferromagnetism and metallicity in the $CaMn_{1-x}Ru_xO_3$ perovskites: a highly inhomogeneous system, *Solid State Commun.*, 2001, **17**, 377.

17 Y. Hinatsu, Y. Izumiyama, Y. Doi, A. Alemi, M. Wakeshima, A. Nakamura and Y. Morii, Studies on magnetic and calorimetric properties of double perovskites Ba_2HoRuO_6 and Ba_2HoIrO_6, *J. Solid State Chem.*, 2004, **177**, 38.

18 Y. Doi and Y. Hinatsu, Crystal structures and magnetic properties of ordered perovskites Sr_2LnRuO_6 (Ln = Eu–Lu), *J. Phys.: Condens. Matter*, 1999, **11**, 4813.

19 P. D. Battle, C. W. Jones and F. Studer, The Crystal and Magnetic Structures of Ca_2NdRuO_6, Ca_2HoRuO_6, and Sr_2ErRuO_6, *J. Solid State Chem.*, 1991, **90**, 302.

20 J. C. Dyre, The random free∼energy barrier model for ac conduction in disordered solids, *J. Appl. Phys.*, 1988, **64**, 2456.

21 K. L. Ngai and C. T. Moynihan, The Dynamics of Mobile Ions in Ionically Conducting Glasses and Other Materials, *Mater. Res. Soc. Bull.*, 1998, **23**, 51.

22 A. K. Jonscher, The universal dielectric response, *Nature*, 1977, **267**, 673.

23 D. P. Almond and A. R. West, Anomalous conductivity prefactors in fast ion conductors, *Nature*, 1983, **306**, 456.

24 B. Roling and C. Martiny, Non-universal Features of the ac Conductivity in Ion Conducting Glasses, *Phys. Rev. Lett.*, 2000, **85**, 1274.

25 R. Murugaraj, G. Govindaraj and D. George, AC conductivity and its scaling behavior in lithium and sodium bismuthate glasses, *Mater. Lett.*, 2003, **57**, 1656.

26 S. Saha and T. P. Sinha, Low-temperature scaling behavior of $BaFe_{0.5}Nb_{0.5}O_3$, *Phys. Rev. B: Condens. Matter Mater. Phys.*, 2002, **65**, 134103.

27 P. Singh, R. Pandey, O. Parkash and D. Kumar, Scaling of low-temperature conductivity spectra of $BaSn_{1-x}Nb_xO_3$ ($x \leq 0.100$): Temperature and compositional-independent conductivity, *Phys. Rev. B: Condens. Matter Mater. Phys.*, 2011, **84**, 174306.

28 S. Murugavel and B. Roling, ac Conductivity Spectra of Alkali Tellurite Glasses: Composition-Dependent Deviations from the Summerfield Scaling, *Phys. Rev. Lett.*, 2002, **89**, 195902.

29 H. Kahnt, Ionic Transport in Oxide Glasses and Frequency Dependence of Conductivity, *Ber. Bunsen-Ges.*, 1991, **95**, 1021.

30 B. Roling, A. Happe, K. Funke and M. D. Ingram, Carrier Concentrations and Relaxation Spectroscopy: New Information from Scaling Properties of Conductivity Spectra in Ionically Conducting Glasses, *Phys. Rev. Lett.*, 1997, **78**, 2160–2163.

31 D. L. Sidebottom, Universal Approach for Scaling the ac Conductivity in Ionic Glasses, *Phys. Rev. Lett.*, 1999, **82**, 3653.

32 S. D. Baranovskii and H. Corder, On the conduction mechanism in ionic glasses, *J. Chem. Phys.*, 1999, **111**, 7546.

33 J. Rodriguez-Carvajal, Recent advances in magnetic structure determination neutron powder diffraction, *Phys. B*, 1993, **192**, 55.

34 R. Mukherjee, A. Dutta and T. P. Sinha, Dielectric Relaxation of Rare Earth Ordered Double Perovskite Oxide Ba_2ErTaO_6, *J. Electron. Mater.*, 2016, **45**, 846.

35 G. Y. Liu, G. H. Rao, X. M. Feng, H. F. Yang, Z. W. Ouyang, W. F. Liu and J. K. Liang, Atomic ordering and magnetic properties of non-stoichiometric double-perovskite $Sr_2FexMo_{2-x}O_6$, *J. Phys.: Condens. Matter*, 2003, **15**, 2053.

36 P. M. Woodward, R. D. Hoffman and A. W. Sleight, Order-disorder in $A_2M^{3+}M^{5+}O_6$ perovskites, *J. Mater. Res.*, 1994, **9**, 2118.

37 W. T. Fu and D. J. W. Ijdo, X-ray and neutron powder diffraction study of the monoclinic perovskites Sr_2MSbO_6 (M = In, Y), *Solid State Commun.*, 2005, **134**, 177.

38 S. Halder, A. Dutta and T. P. Sinha, Dielectric relaxation and electrical conduction mechanism in A_2HoSbO_6 (A = Ba, Sr, Ca) Double Perovskite Ceramics: An impedance spectroscopic analysis, *J. Phys. Chem. Solids*, 2017, **102**, 79.

39 P. J. Saines, B. J. Kennedy and M. M. Elcombe, Structural phase transitions and crystal chemistry of the series $Ba_2LnB'O_6$ (Ln = lanthanide and B′ = Nb^{5+} or Sb^{5+}), *J. Solid State Chem.*, 2007, **180**, 401.

40 H. D. Megaw, Crystal structure of double oxides of the perovskite type, *Proc. Phys. Soc.*, 1946, **58**, 133.

41 H. D. Megaw, *Crystal Structures: A Working Approach*, W. B. Saunders Company, London, 1973.

42 D. P. Almond and A. R. West, Impedance and Modulus spectroscopy of Real dispersive conductors, *Solid State Ionics*, 1983, **11**, 57.

43 D. P. Almond, G. K. Ducan and A. R. West, The Determination of Hopping Rates and Carrier Concentrations in Ionic Conductors by a new analysis of ac conductivity, *Solid State Ionics*, 1983, **8**, 159.

44 K. Funke, B. Heimann, M. Vering and D. Wilmer, Concept of Mismatch and Relaxation Explains DC and AC Conductivities of Fragile Glass-Forming Ionic Melts, *J. Electrochem. Soc.*, 2001, **148**, 395.

45 D. A. Payne and L. E. Cross, *Microstructure-Property Relations for Dielectric Ceramics: II. The Brick-Wall Model of Polycrystalline Microstructure Microstructure and Properties of Ceramic Materials*, 1984, vol. 380.

46 R. Waser, Bulk Conductivity and Defect Chemistry of Acceptor-Doped Strontium Titanate in the Quenched State, *J. Am. Ceram. Soc.*, 1991, **74**, 1934.

47 M. Vollman and R. Waser, Grain Boundary Defect Chemistry of Acceptor-Doped Titanates: Space Charge Layer Width, *J. Am. Ceram. Soc.*, 1994, **77**, 235.

48 K. Funke, Jump relaxation in solid electrolytes, *Prog. Solid State Chem.*, 1993, **22**, 111.

49 A. A. Youssef Ahmed, The Permittivity and AC Conductivity of the Layered Perovskite $[(CH_3)(C_6H_5)_3P]_2HgI_4$, *Z. Naturforsch.*, 2002, **57**, 263.

50 J.-S. Zhou, K. Matsubayashi, Y. Uwatoko, C.-Q. Jin, J.-G. Cheng, J. B. Goodenough, Q. Q. Liu, T. Katsura, A. Shatskiy and E. Ito, Critical Behavior of the Ferromagnetic Perovskite $BaRuO_3$, *Phys. Rev. Lett.*, 2008, **101**, 077206.

51 B. Szymanik and A. Edgar, Electrical Conductivity of $BaRuO_3$ Ceramics, *Solid State Commun.*, 1991, **79**, 355.

52 A. Ito, H. Masumoto and T. Goto, Microstructure and Electrical Conductivity of $CaRuO_3$ Thin Films Prepared by Laser Ablation, *Mater. Trans.*, 2008, **49**, 158.

53 V. Markovich, M. Auslender, I. Fita, R. Puzniak, C. Martin, A. Wisniewski, A. Maignan, B. Raveau and G. Gorodetsky, Interplay between itinerant and localized states in $CaMn_{1-x}RuxO_3$ ($x \leq 0.5$) manganites, *Phys. Rev. B: Condens. Matter Mater. Phys.*, 2006, **73**, 014416.

54 V. Vashook, D. Nitsche, L. Vasylechko, J. Rebello, J. Zosel and U. Guth, Solid state synthesis, structure and transport properties of compositions in the $CaRu_{1-x}Ti_xO_{3-\delta}$ system, *J. Alloys Compd.*, 2009, **485**, 73.

55 H. Rahmouni, R. Jemai, M. Nouiri, N. Kallel, F. Rziguac, A. Selmi, K. Khirouni and S. Alayaa, Admittance spectroscopy and complex impedance analysis of Ti-modified $La_{0.7}Sr_{0.3}MnO_3$, *J. Cryst. Growth*, 2008, **310**, 556.

56 J. Yang, B. C. Zhao, Y. Q. Ma, R. L. Zhang, R. Ang, W. H. Song and Y. P. Sun, Small-polaron hopping conduction in $La_{0.9}Te_{0.1}MnO_3$ above the metal-insulator transition, *Mater. Lett.*, 2006, **60**, 3281.

57 O. N. Verma, N. K. Singh, R. Pandey and P. Singh, Study of ion dynamics in lanthanum aluminate probed by conductivity spectroscopy, *RSC Adv.*, 2015, **5**, 21614.

58 N. F. Mott and E. A. Davis, *Electronic Processes in Noncrystalline Materials*, Clarendon, Oxford, 1979.

59 P. N. Vishwakarma and S. V. Subramanyam, Hopping conduction in boron doped amorphous carbon films, *J. Appl. Phys.*, 2006, **100**, 113702.

60 A. K. Biswal, J. Ray, P. D. Babu, V. Siruguri and P. N. Vishwakarma, Dielectric relaxations in La_2NiMnO_6 with signatures of Griffiths phase, *J. Appl. Phys.*, 2014, **115**, 194106.

61 S. Summerfield, Universal low-frequency behaviour in the a.c. hopping conductivity of disordered systems, *Philos. Mag. B*, 1985, **52**, 9.

62 A. Ghosh and A. Pan, Scaling of the Conductivity Spectra in Ionic Glasses: Dependence on the Structure, *Phys. Rev. Lett.*, 2000, **84**, 2188.

63 A. Ghosh and M. Sural, Conductivity spectra of sodium fluorozirconate glasses, *J. Chem. Phys.*, 2001, **114**, 3243.

64 C. R. Mariappan, AC conductivity scaling behaviour in grain and grain boundary response regime of fast lithium ionic conductors, *Appl. Phys. A*, 2014, **117**, 847.

65 P. B. Macedo, C. T. Moynihan and R. Bose, Role of ionic diffusion in polarization in vitreous ionic conductors, *Phys. Chem. Glasses*, 1972, **13**, 171.

66 I. M. Hodge, M. D. Ingram and A. R. West, Impedance and modulus spectroscopy of polycrystalline solid electrolytes, *J. Electroanal. Chem.*, 1976, **74**, 125.

67 G. M. Tsangaris, G. C. Psarras and N. Kouloumbi, Electric modulus and interfacial polarization in composite polymeric systems, *J. Mater. Sci.*, 1998, **33**, 2027.

68 S. Halder, M. S. Sheikh, B. Ghosh and T. P. Sinha, Electronic structure and Electrical conduction by polaron hopping mechanism in A_2LuTaO_6 (A = Ba, Sr, Ca) Double Perovskite Oxides, *Ceram. Int.*, 2017, **43**, 11097.

69 M. Bakr Mohamed, H. Wang and H. Fuess, Dielectric relaxation and magnetic properties of Cr doped $GaFeO_3$, *J. Phys. D: Appl. Phys.*, 2010, **43**, 455409.

70 J. M. Bobe, J. M. Reau, J. Senegas and M. Poulain, F-ion conductivity and diffusion properties in ZrF_4-based fluoride glasses with various NaF concentrations ($0 < x$NaF < 0.45), *Solid State Ionics*, 1995, **82**, 39.

71 J. R. Macdonald, Scaling and modeling in the analysis of dispersive relaxation of ionic materials, *J. Appl. Phys.*, 2001, **90**, 153.